Defective Bi_4MoO_9/Bi metal core/shell heterostructure: Enhanced visible light photocatalysis and reaction mechanism

Wenjie He[a], Yanjuan Sun[a], Guangming Jiang[a,*], Yuhan Li[a], Xianming Zhang[a], Yuxin Zhang[b], Ying Zhou[c], Fan Dong[a,c,*]

[a] Chongqing Key Laboratory of Catalysis and New Environmental Materials, Engineering Research Center for Waste Oil Recovery Technology and Equipment of Ministry of Education, College of Environment and Resources, Chongqing Technology and Business University, Chongqing 400067, China
[b] College of Materials Science and Engineering, Chongqing University, Chongqing 400044, China
[c] The Center of New Energy Materials and Technology, School of Materials Science and Engineering, Southwest Petroleum University, Chengdu 610500, China

ABSTRACT

Bi_4MoO_9 is a promising photocatalyst for air pollutant mineralization due to its very positive valance band edge at 3.48 eV. However, its performance usually suffers from its wide band gap and high charge recombination rate, which limits its scaled application. To address these issues, one novel Bi_4MoO_9/Bi° core/shell heterostructured photocatalyst with considerable number of oxygen vacancies was synthesized through a facile surface chemical reduction treatment over the pre-synthesized Bi_4MoO_9 microrods in $NaBH_4$ aqueous solution. The combined TEM/HRTEM, UV–vis DRS, PL and ESR study reveals that the construction of Bi_4MoO_9/Bi° heterojunction in the core/shell structure, the surface plasmon resonance (SPR) of Bi metal and the oxygen vacancy-induced formation of defect states all contribute to an intensified photoabsorption, charge separation efficiency and generation of oxidative radicals. The photocatalytic NO removal test under visible light irradiation shows that Bi_4MoO_9/Bi°-40 (40 denotes the molar ratio of $NaBH_4$ to Bi_4MoO_9 is 40/60) presents a maximum NO removal efficiency of 55.4%, much higher than that of the original Bi_4MoO_9 (12.7%). The reaction pathway of the photocatalytic NO oxidation over the Bi_4MoO_9/Bi° was examined by in-situ DRFTS and the NO^+ species as a kind of intermediate product in NO conversion is detected and critical for the conversion of NO to nitrate. The present work provides a new approach to activate the non-visible-light response semiconductor for efficient visible light photocatalysis.

1. Introduction

Environmental pollution and energy shortage are becoming austere issues [1–4]. As one effective and environmental-friendly technology towards pollutant mineralization, visible-light-driven photocatalysis is rapidly developed [5–10]. Bismuth molybdates, the key member of the Aurivillius oxide family, is regarded as one of the most promising photocatalysts due to the decent intrinsic merits, such as the tunable band gap for visible light excitation [11,12] and the tunable morphology [13–16]. They are featured with a crystal structure composed of accumulated layers of alternating bismuth oxide $(BiO)^+$ layers and octahedral molybdate sheets, and have various crystalline phases, such as γ-Bi_2MoO_6, $Bi_{3.64}Mo_{0.36}O_{6.55}$ and Bi_4MoO_9 [17–19] of which Bi_4MoO_9 is attracting ever-growing attention due to its very positive valance band edge at 3.48 eV. However, the high charge recombination rate and a wide band gap of Bi_4MoO_9 limit its scaled application.

To promote the charge separation, various strategies have been developed, including i) building a heterojunction [20,21], ii) introducing a metal with SPR effect [22,23] and iii) constructing oxygen vacancy [24,25]. Fortunately, the core/shell [26–30] structure could both enhance the photoabsorption and promote the separation of hole/electrons pairs. Nobel metal was usually employed as the surface modification cocatalyst and plays the role of shell in core/shell structure. As is known, it is essential to decrease the cost for the industrialization of the catalyst. The good news is that non-noble metallic bismuth has been discovered to exhibit a direct plasmonic photocatalytic ability, and extensively used as cocatalyst to reinforce the visible light adsorption and promote charge separation [31], so that metallic Bi is regarded as a promising candidate to replace Au and Ag. Nanoscale metallic Bi has been coupled with various photocatalysts,

such as BiOCl [32], $(BiO)_2CO_3$ [33], and g-C_3N_4 [34]. Undeniably, these Bi load nanocomposites conspicuously improved photocatalytic performance when compared with individual components. In addition, oxygen vacancy, the most general defect in oxide semiconductors, which is the electrons enrichment sites established the defect states like a ladder within the band gap. The formed defect states could offer an initial condition to transfer electrons department in activity radical species generation [35,36].

In this work, we developed one novel core/shell heterostructure with the Bi_4MoO_9 rod as the core and $Bi°$ phase as the shell through a surface chemical reduction treatment over pre-synthesized Bi_4MoO_9 microrods by $NaBH_4$. Fortunately, this chemical reduction treatment will also introduce considerable number of oxygen vacancy in the composite. As expected, the $Bi_4MoO_9/Bi°$ exhibited highly enhanced photocatalytic activity and durability to remove ppb-level NO under visible light irradiation in comparison to the pure Bi_4MoO_9. In addition, a photocatalytic NO oxidation mechanism on $Bi_4MoO_9/Bi°$ was proposed based on the UV–vis DRS, PL and ESR analyses and the *in-situ* observation of the reaction intermediates by DRTFIS. Overall, the present work will pave a way for utilizing the non-noble metal to enhance the semiconductor photocatalyst for practical applications.

2. Experimental

2.1. Catalyst preparation

All the chemicals are of analytical grade and used without further purification. The $Bi_4MoO_9/Bi°$ composites were prepared by a facile *in-situ* wet-chemical reduction method with pure Bi_4MoO_9 as the substrate. The Bi_4MoO_9 was obtained by a hydrothermal method: 1.455 g of $Bi(NO_3)_3 \cdot 5H_2O$ was added to 30 mL of HNO_3 (1 mM), and dispersed by ultra-sonication and magnetic stirring for 10 min, forming a homogenous white suspension. Then, 0.267 g of $(NH_4)_6Mo_7O_{24} \cdot 4H_2O$ pre-dissolved in 30 mL of deionized water and 3 ml of Oleylamine was in sequence dropwise added into mixture suspension, after that the pH was adjusted to 7 by using NaOH solution (2 M). After being stirred for 1 h at room temperature, the suspension was transferred into a 100 mL Teflon-lined stainless autoclave and kept reaction at 160 °C for 24 h. After cooling to the room temperature, the product was washed repeatedly by deionized water and ethanol, and then dried at 120 °C for further use.

The core/shell $Bi_4MoO_9/Bi°$ samples were then synthesized by using the above Bi_4MoO_9 as the precursor and $NaBH_4$ solution as the reducing agent. By controlling the ratio of $NaBH_4$ to Bi_4MoO_9, series of $Bi_4MoO_9/Bi°$ with different contents of Bi could be obtained. In detail, 1.0 g of pure Bi_4MoO_9 powders and 2.0 g of Polyvinyl Pyrrolidone were added into 100 mL of deionized water with a further continuous stirring for 30 min. Then, 20 mL of $NaBH_4$ solution with different $NaBH_4/Bi_2WO_6$ molar ratios of 0.2, 0.4 and 0.6 was dropwise added into the Bi_4MoO_9 suspensions, respectively. After reaction for 1 h the products were collected, washed with deionized water and absolute ethanol for twice and then dried at 40 °C for 12 h in a Drying Oven. According to the $NaBH_4/Bi_4MoO_9$ molar ratio of 20/80, 40/60 and 60/40, the products were denoted as BM-20, BM-40 and BM-60, respectively.

2.2. Characterization

The crystal phase of Bi_2WO_6 was analyzed by X-ray diffraction (XRD) with Cu Kα radiation (model D/max RA, Rigaku Co., Japan). X-ray photoelectron spectroscopy (XPS) with Al Kα X-rays ($h\nu = 1486.6$ eV) radiation operated at 150 W (Thermo ESCALAB 250, USA) was used to investigate the surface properties. Scanning electron microscopy (SEM, model JSM-6490, JEOL, Japan) and transmission electron microscopy (TEM, JEM-2010, JEOL, Japan) were used to characterize the morphology and structure of Bi_2WO_6. N_2 adsorption-desorption isotherms were obtained on N_2 adsorption apparatus (ASAP

2020, Micromeritics, USA). The UV–vis diffuse-reflectance spectrometry (UV–vis DRS) spectrum was obtained for the dry-pressed disk samples using a scanning UV–vis spectrophotometer (TU-1901, China) equipped with an integrating sphere assembly, using 100% $BaSO_4$ as the reflectance sample. Steady and time-resolved fluorescence emission spectra were recorded at room temperature with a fluorescence spectrophotometer (Edinburgh Instruments, FLSP-920). The sample for ESR measurement (FLsp920, U.K.) was prepared by mixing Bi_2WO_6 in a 50 mM DMPO solution with aqueous dispersion for DMPO$-\cdot$OH and methanol dispersion for DMPO$-\cdot O_2^-$. In situ DRIFTS measurements (VERTEX70 FTIR spectrometer, Bruker) equipped with an in situ diffuse-reflectance cell (Harrick) were conducted to understand the related photocatalytic oxidation processes over catalyst.

2.3. Visible light photocatalytic NO removal

The photocatalytic activity was evaluated by the removal efficiency of NO at ppb levels in a continuous flow reactor at ambient temperature. The rectangular reactor (30 cm × 15 cm × 10 cm) is made of polymeric glass and covered with Saint-Glass. A commercial tungsten halogen lamp (150 W) was vertically placed outside and 20 cm above the reactor. The UV light in the light beam was removed by adopting a UV cutoff filter (420 nm). The as-prepared sample (0.20 g) was dispersed in absolute ethyl alcohol (25 mL) via ultrasonic treatment. The resulting suspension was coated onto two glass dishes (12.00 cm in diameter) and then pretreated at 55 °C to remove ethyl alcohol. The NO gas acquired from a compressed gas cylinder at a concentration of 100 ppm of NO (N_2 balance). The initial concentration of NO was diluted to about 550 ppb by a zero air generator. And the relative humidity (RH) level of the NO flow was controlled at 50% by passing the air stream through a humidification chamber. The flow rates of the air stream and NO were controlled at 2.4 L/min and 15 mL/min, respectively. The lamp was turned on when the adsorption-desorption equilibrium was achieved. The concentration of NO was continuously measured by a NO_X analyzer (Thermo Environmental Instruments Inc., model 42c-TL), which can monitor the concentration of NO, NO_2 and NO_X (NO_X represents NO + NO_2). The removal ratio (η) of NO was calculated as $\eta = (1 - C/C_0) \times 100\%$, where C and C_0 are the concentrations of NO in the outlet steam and the feeding stream, respectively.

2.4. In situ DRIFT investigation

In situ DRIFTS experiments were carried out by using Bruker Tensor 27 DRIFTS spectrometers. Catalysts were pretreated at room temperature under He (30 mL min^{-1}) for 60 min to remove adsorbed impurities. After the background spectrum was recorded with the flowing of He and was subtracted, the samples were then exposed to 300 ppm of NO with 20% O_2. DRIFTS spectra of samples were recorded at room temperature by accumulating 32 scans with a resolution of 4 cm^{-1} at a given interval. The original DRIFTS data was normalized to intuitionally evaluate the species evolution. For a specific species on $Bi_4MoO_9/Bi°$-40, the data of peak heights were respectively extracted for sample. Among the columns of data, the highest value was set to be 1 and the lowest value was set to be 0. The rest were correspondingly normalized from 0 to 1. The resulted normalized data were thus described as a function of the DRIFTS scanning time (Fig. 1).

3. Results and discussion

3.1. Synthesis of the core/shell $Bi_4MoO_9/Bi°$ microrods

The core/shell $Bi_4MoO_9/Bi°$ microrods were synthesized by immersing the as-synthesized Bi_4MoO_9 powders into a $NaBH_4$ aqueous solution, which leads to reduction of the surface Bi^{3+} of Bi_4MoO_9 to $Bi°$ and the *in-situ* growth of $Bi°$ phase over the surface of Bi_4MoO_9 microrods. The low magnification TEM of BM and BM-40 shown in Fig.
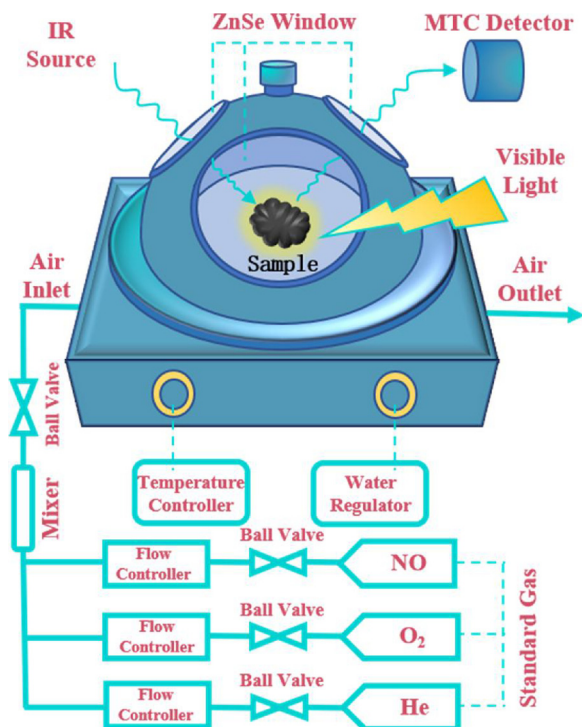
Fig. 1. Scheme of the in situ DRIFTS analysis cell equipped with a visible light illumination.

S1. And Fig. 2a shows one typical TEM image of the as-synthesized solid Bi_4MoO_9, which clearly present a rod shape with distinct surface/edges and a width of 0.8 μm. After reduction by $NaBH_4$, the rod shape is preserved, but some fish scaly-like structure encapsulates the rod, with a thickness of around 0.1 μm. Further HRTEM examination finds one clear (111) spacings of 3.270 Å on the microrod surface of the pure Bi_4MoO_9, while three more lattice spacings of 2.030 Å, 2.273 Å and 3.280 Å on the surface layered structure of $Bi_4MoO_9/Bi°$ sample, which can be indexed to (015), (110) and (012) crystal planes of metallic Bi phase. The Bi_4MoO_9 is indicated to be preserved in $Bi_4MoO_9/Bi°$ composite by the clear (220) spacing of 1.994 Å. All these demonstrate the successful synthesis of the core/shell $Bi_4MoO_9/Bi°$ microrods with a rod-shaped Bi_4MoO_9 core and a hierarchical fish scaly-like $Bi°$ shell.

To explore more about the chemical composition in $Bi_4MoO_9/Bi°$, X-ray photoelectron spectroscopy (XPS) analyses were conduced. The XPS survey spectra of Bi_4MoO_9 and $Bi_4MoO_9/Bi°$ in Fig. 3a both show the signals of the elements Bi, Mo, O and C elements, and no other elements, such as B and Na, are discerned, indicating the high purity of the products. After sputtering of the sample BM-40 surface for 30 nm, the signal of C element disappeared, confirming that the element C is adventitious. The high-resolution XPS spectra of three constituent elements Bi, Mo and O in Bi_4MoO_9 and $Bi_4MoO_9/Bi°$-Ar (-Ar denotes utilize Ar ion sputtering 30 nm depth on the sample surface) are compared in Fig. 3b–d. After checking the Bi $4f_{7/2}$ and Bi $4f_{5/2}$ characteristic peaks in Fig. 3b, it is observed that the Bi^{3+} is detected in both the Bi_4MoO_9 and $Bi_4MoO_9/Bi°$-Ar (See the binding energy peak at 158.8 eV and 164.1 eV), while the $Bi°$ phase is only visible in $Bi_4MoO_9/Bi°$-Ar (See the binding energy peak at 162.3 eV and 157 eV), confirming the
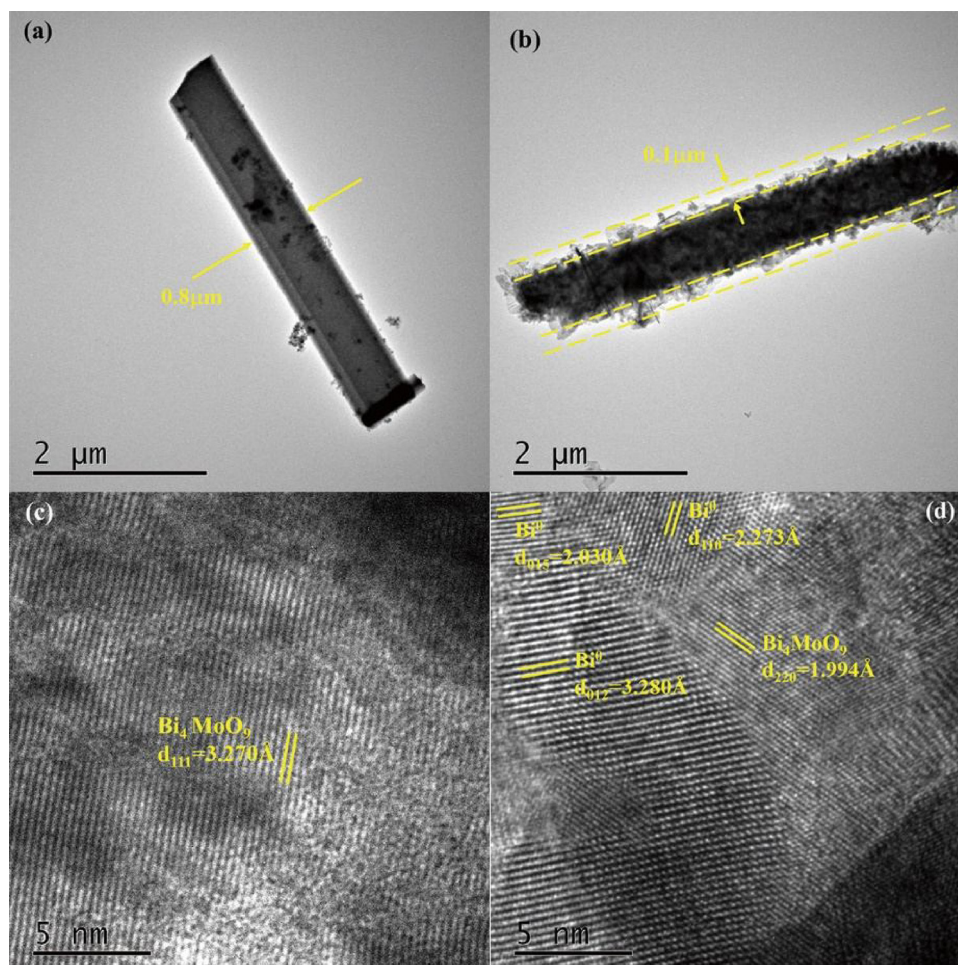

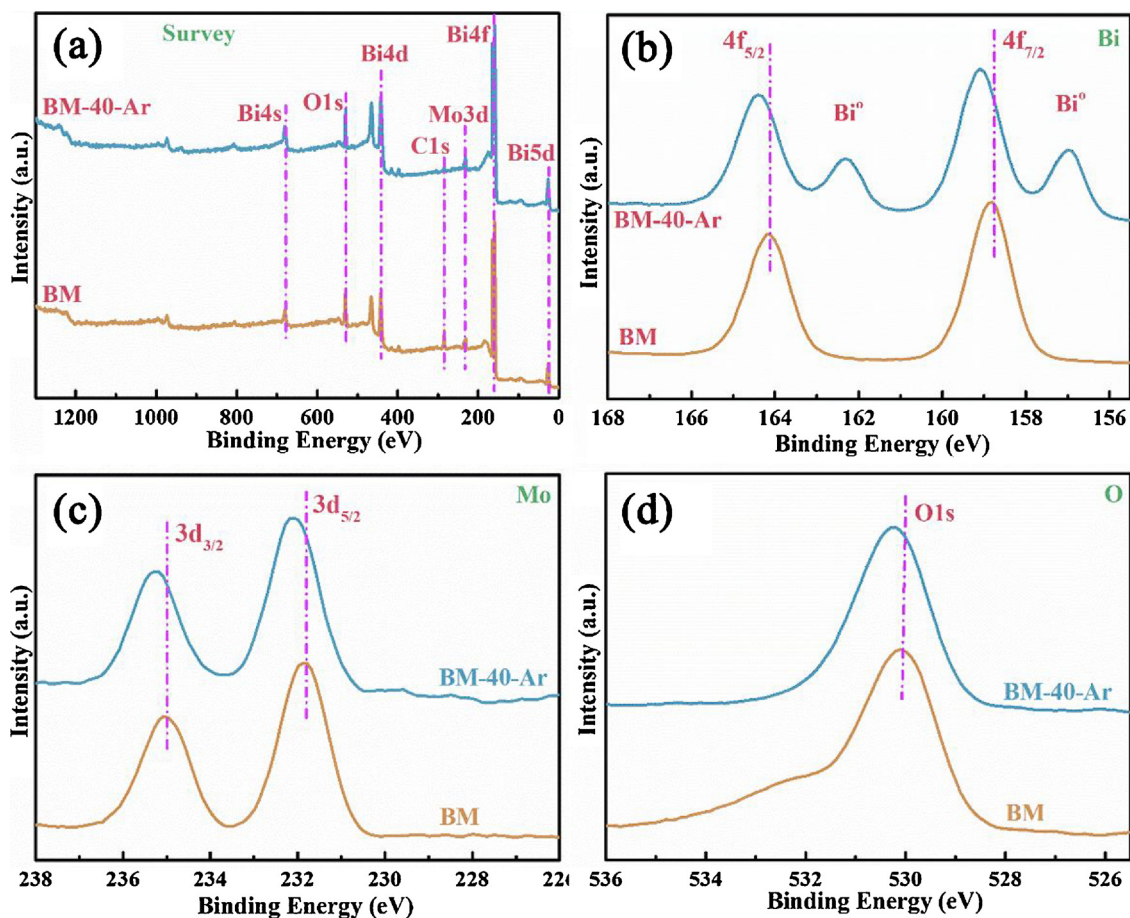**Fig. 2.** The TEM images of BM (a) and BM-40 (b), the HRTEM images of BM (c) and BM-40 (d).

Fig. 3. XPS spectra of Bi–BWO: survey (a), Bi 4f (b), Mo 3d (c), O 1s (d).

formation of Bi° in $Bi_4MoO_9/Bi°$-Ar, which is consistent with the HRTEM results in Fig. 2d. The Mo $3d_{5/2}$ and Mo $3d_{3/2}$ are shown in the Fig. 3c. Mo^{6+} peaks are detected at 231.88 eV and 235.08 eV in both the Bi_4MoO_9 and BM-40-Ar, and no metallic Mo phase or Mo^{3+} is visible. However, Fig. 3b–c shows that the peak of Bi^{3+} is shifted to a higher binding energy, which can be attributed to the oxygen vacancy that could attract the surrounding electrons. The shift of the Mo 3d binding energy can be ascribed to the interaction between Bi metal and Bi_4MoO_9. The O 1s peak XPS spectra of Bi_4MoO_9 in Fig. 3d shows the O 1s peak also shifts, which could be ascribed to the fact that the chemical environment of O element has been changed.

Since the Bi° is reduced from Bi^{3+} by $NaBH_4$, the amount of Bi° in the core/shell structure can be tuned by the concentration of the $NaBH_4$ aqueous solution. Fig. 4 shows the XRD patterns of the $Bi_4MoO_9/Bi°$ composites those evolve with the molar ratio of $NaBH_4$ to Bi_4MoO_9 (denoted as X below). The results in Fig. 4 show that the as-synthesized Bi_4MoO_9 presents the typical diffraction peaks of the face-centered cubic Bi_4MoO_9 phase (JCPDS No.12-0149) at $2\theta = 27.2°$, $31.6°$, $45.4°$ and $53.9°$. With an increase in $NaBH_4$ dosage, the characteristic peaks of Bi_4MoO_9 changes little, indicating the reduction process will not destroy the crystalline structure of Bi_4MoO_9. The Bi° is detectable by its two weak diffraction peaks appear at $2\theta = 38.0°$ and $39.6°$ when the X reaches 60. These results confirm that the Bi° phase (JCPDS No.05-0519) can be formed over Bi_4MoO_9 via a reductive reaction of Bi_4MoO_9 with $NaBH_4$. The undetected Bi° phase in BM-20 and 40 may be ascribed to its low amount when less $NaBH_4$ is added.

3.2. Photocatalytic performance

The photocatalytic performance of Bi_4MoO_9 and BM-X (X = 20, 40

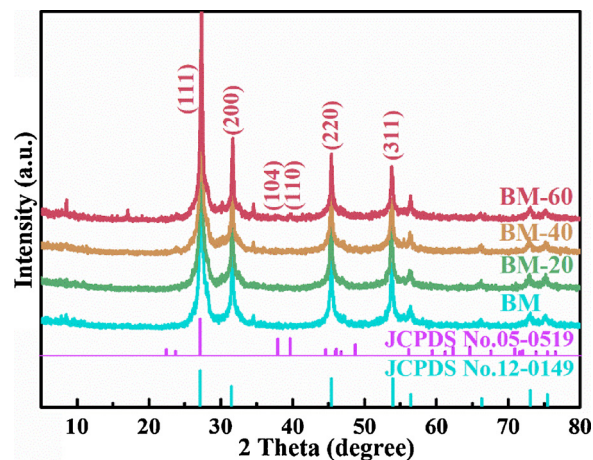**Fig. 4.** The XRD pattern of pure Bi_4MoO_9 and BM-X (X = 20, 40, 60).

and 60) were evaluated via its activity in removing NO from a continuous air flow under visible light irradiation, and the activity was assessed by the ratio of NO concentration in outlet stream (C) to that in feeding stream (C_0). A lower ratio means that more NO has been removed, and the corresponding sample thus has a higher photocatalytic activity. Fig. 5a shows that the $C/C°$ decreases for all the samples, indicating all of them are active for NO removal under the visible light illumination. Fig. 5b presents the stabilized removal efficiency [(1- $C/C°$)×100%] of all the samples, which clearly shows that the BM-X have a much higher NO removal efficiency than Bi_4MoO_9. Furthermore, with an increase in the X, BM-X (X = 20, 40 and 60) shows an increased NO

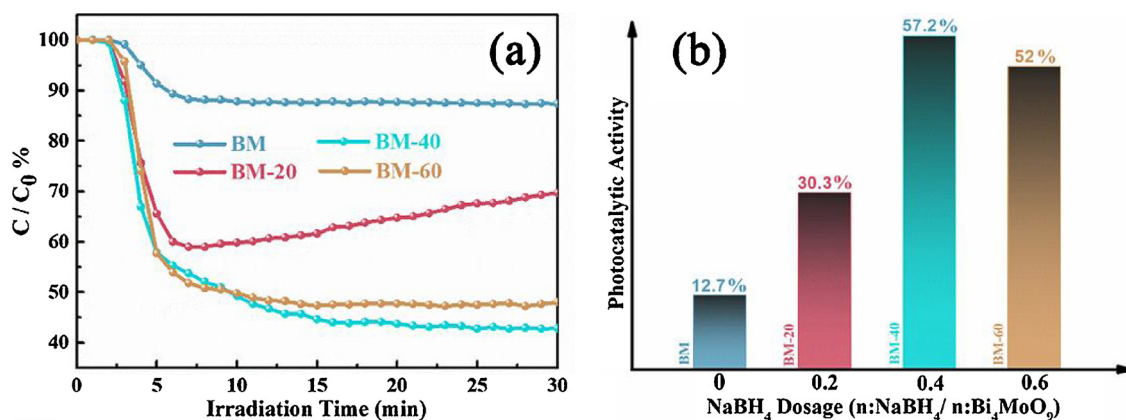**Fig. 5.** The concentration of NO changed with time over pure Bi_4MoO_9 and BM-X(X = 20, 40, 60) for NO removal (a) and the Visible light photocatalytic activities relative to the dosage of $NaBH_4$ after 30 min (b).

removal efficiency, reaches peak of 57.2% at X = 40, and then decreases. The results suggest that the Bi deposition can significantly improve the photocatalytic performance of Bi_4MoO_9, but two much $Bi°$ covering the Bi_4MoO_9 will deteriorate the activity of the sample. Note that the sample BM-20 showed slight deactivation during the irradiation because its microstructure has not been fully optimized. The $Bi°/Bi_4MoO_9$ demonstrated much efficient activity in comparison with noble metal (Au, Ag, Pd) decorated Bi_4MoO_9 due to appropriate work function of Bi metal (Figs. S6 and S7). In this sense, the metallic Bi with SPR property is a good substitute of other noble metals as cocatalyst. Fig. S2 presents the result of circulating runs of BM-40 in photocatalytic NO removal, which indicates that the sample is durable for a least five cycles.

3.3. Charge generation and transfer

The light absorption intensity and the separation efficiency of hole/electron pairs are two well-known critical factors determining the photocatalytic performance. The UV–vis diffuse reflectance spectra (DRS) of Bi_4MoO_9 and BM-X (X = 20, 40, 60) presented in Fig. 6a show that the BM-X with a larger X has a stronger visible light absorption. The absorption enhancement should originate from the SPR effect of metallic $Bi°$ phase, and a stronger absorption at a larger X confirms a larger number of Bi phase in BM-X. To examine the charge mobility in the sample, the ns-level time-resolved fluorescence spectra of BM and BM-40 are typically compared in Fig. 6b. The biexponential decay function is utilized to fit the curves (Table 1). Interestingly, the shorter lifetime of $\tau_1 = 1.5982$ ns are observed for BM-40, in comparison with that of $\tau_1 = 2.0221$ ns for the pure Bi_4MoO_9, which demonstrates that the $Bi°$ phase can effectively shorten the lifetime of photogenerated electrons. Combined with the increased electron-transfer rate (ΔK_{ET}) in BM-40 over that in BM, it is suggested that the constructed heterojunction between metallic Bi and Bi_4MoO_9 planes can efficiently direct the electron transfer between Bi and in Bi_4MoO_9, and promote the electron-hole separation by directing the electron moving towards Bi phase. The enhanced electron–hole separation in BM-X is further confirmed by the Fluorescence Spectroscopy. The results in Fig. 6c shows the peak intensity of BM-40 and BM-60 decreased drastically, which further demonstrates that the introduction of metallic Bi can significantly hinder the recombination of photogenerated electron hole pairs. The strong fluorescence spectrum of sample BM-20 revealed it suffered the high hole/electron recombination efficiency. It is perfectly matched with the photocatalysis activity test of NO oxidation over sample BM-20 which the concentration of outlet NO was continuous increasing, as the results that the low dosage reductant produced metallic Bi is unstable.

$$\Delta KET = \frac{1}{\tau 1(BM-40)} - \frac{1}{\tau 1(BM)} \quad (1)$$

Room temperature solid-state electron paramagnetic resonance spectra (Fig. 6d) are employed to quantify the atom vacancy in Bi_4MoO_9 and BM-40. Both samples show a sole Lorentzian line at a g value of about 2.0 in dark, which was a typical feature of the presence of the oxygen-induced local magnetic field. The EPR intensity of BM-40 is stronger than that of pure Bi_4MoO_9, and further strengthened with a 15-min visible-light irradiation, which reveals that the electrons mobility can be enormously boosted with the partial removal of oxygen atoms. The defect state built by the oxygen vacancy enable more electrons to overcome a wide band gap and transfer from valance band to conduction band, contributing to the generation of more active radical species.

3.4. The role of Bi metal in enhanced production of reactive species

To elucidate the main active radical species responsible for the NO removal during photocatalytic process, spin-trapping ESR analyses over pure Bi_4MoO_9 and BM-40 for $DMPO-\cdot OH$ and $DMPO-\cdot O_2^-$ were conducted, and the results are presented in Fig. 7a-b. No signals could be observed when the system was kept in dark. With the visible light illumination, both the BM and BM-40 exhibit four characteristic peaks of the $DMPO-\cdot O_2^-$ adduct in Fig. 7a. However, the peaks of BM-40 obviously show stronger intensities, indicating that the $\cdot O_2^-$ has been generated via the reduction of O_2 and the metallic Bi could contribute to produce more $\cdot O_2^-$ radical species. However, the signals of the $DMPO-\cdot OH$ over BM-40 have no absolutely change compare with Bi_4MoO_9 after irradiation and the intensities are significantly weaker than $\cdot O_2^-$ signals in Fig. 7b. It means that partial of h^+ prefers to participate in the direct oxidation reaction for the Bi_4MoO_9 system. To further determine the role of active radical species during photocatalysis, the trapping experiments are performed as shown in Fig. S3. Potassium iodide (KI) is utilized as a hole scavenger, and tert-butyl alcohol (TBA) is an effective $\cdot OH$ scavenger. Potassium dichromate ($K_2Cr_2O_7$) is selected as a photoinduced electron scavenger. The NO removal ratio is decreased upon the addition of TBA, validating that $\cdot OH$ radicals are one of the main active species for NO removal. Notably, when the scavenger $K_2Cr_2O_7$ is added, the photocatalytic capability is remarkably inhibited. This phenomenon implies that photoexcited electrons are the crucial factors responsible for of NO removal as the photoexcited electrons could induce the formation of $\cdot O_2^-$ radicals. Meanwhile, when KI is introduced to the reaction system, the photocatalytic removal of NO is also hampered, which suggested that h^+ is also an important active radical in this Bi_4MoO_9/Bi system.

To have a deep understanding of the photocatalytic mechanism, the band structure of our $Bi_4MoO_9/Bi°$ photocatalyst was studied. The
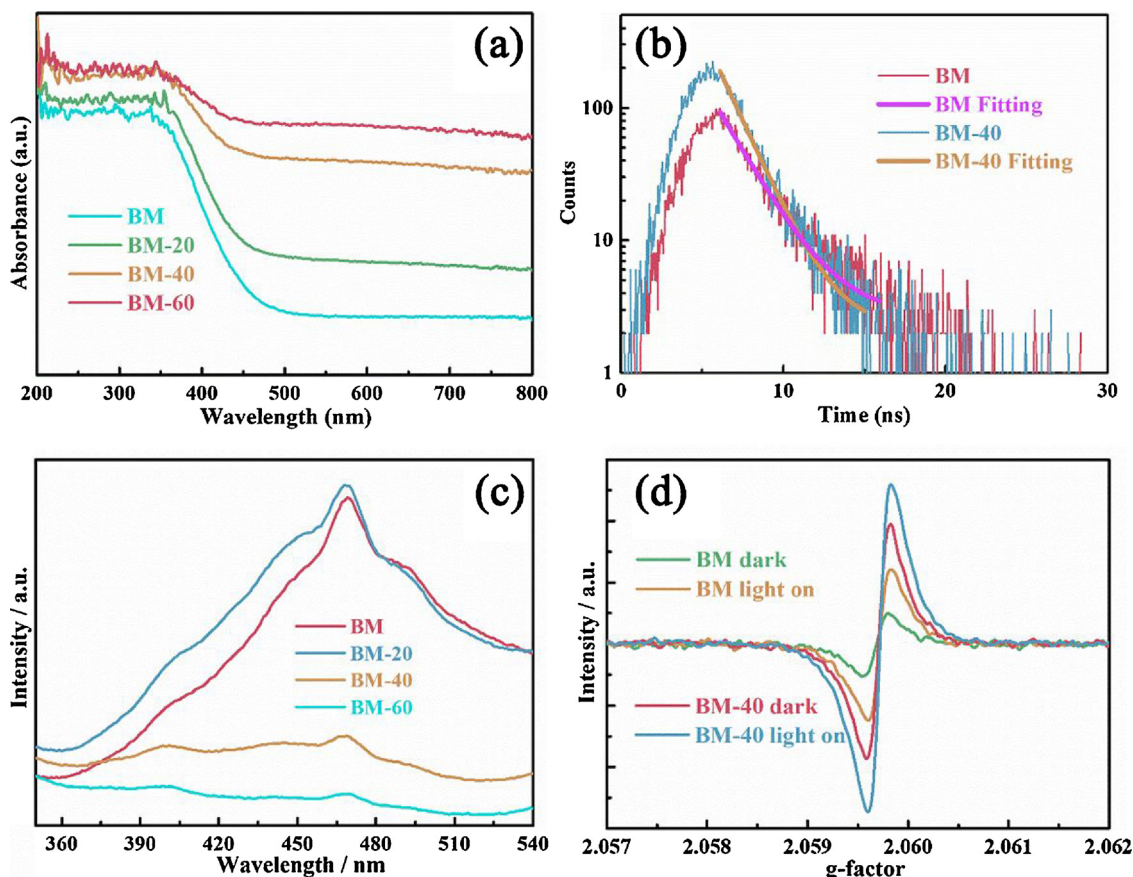
Fig. 6. Optical properties of sample BM and BM-X (X = 20, 40, 60): UV–vis DRS (a),the ns-level time-resolved fluorescence spectrum monitored under 400 nm excitation at room temperature for sample BM and BM-40 (b), the Fluorescence Spectroscopy of BM-X (c) and the room temperature EPR spectra of BM and BM-40 (d).

Table 1
Kinetic parameters for the fitted decay parameters of BM and BM-40.

Sample	Parameter	Lifetime, ns	x^2	ΔK_{ET}[a], ns^{-1}
BM	τ_1	2.0221	0.962	0
BM-40	τ_1	1.5982	1.130	0.1312

[a] ΔK_{ET} refers to the electron-transfer (ET) rate and can be calculated from Eq. (1).

valence band edge position of BM was estimated on the basis the concepts of electronegativity [37,38], where the edge energy of the conducting band (E_{CB}) and valence band (E_{VB}) of a semiconductor can be calculated by the following empirical equation [39]:

$$E_{VB} = X - E^e + 0.5E_g \tag{2}$$

$$E_{CB} = E_{VB} - E_g \tag{3}$$

Where E_g denotes the band gap energy of a semiconductor. X is the electronegativity of the semiconductor, which is the geometric mean of the electronegativity of the constituent atoms, and E^e is the energy of free electrons on the hydrogen scale (about 4.5 eV). The X value of BM is ca. 6.28 eV, and the band gap energy is 3.39 eV (See Fig. S4). Accordingly, the E_{VB} and E_{CB} of BM are estimated to be 3.48 eV and 0.09 eV, respectively.
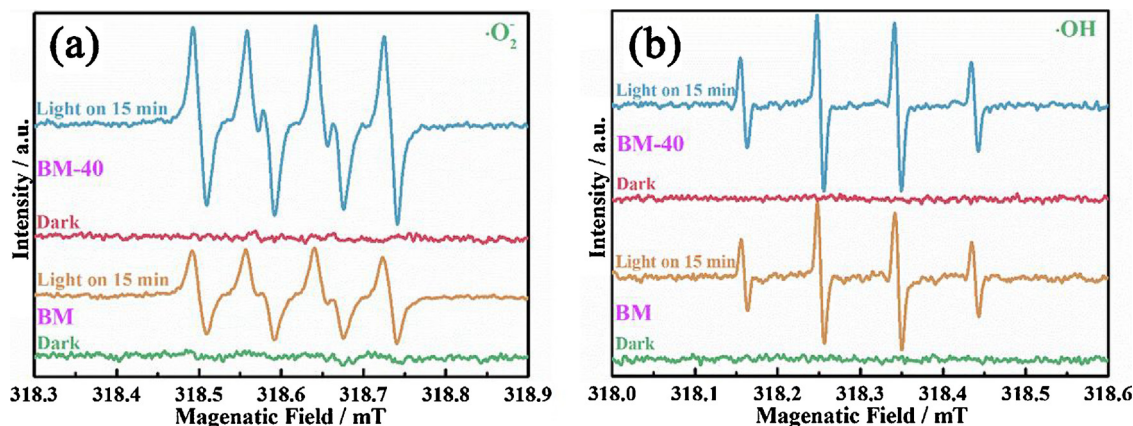

Fig. 7. DMPO spin-trapping ESR spectra of pure Bi_4MoO_9 and BM-40 methanol dispersion for $DMPO-\cdot O_2^-$ (a) and aqueous dispersion for $DMPO-\cdot OH$ (b).

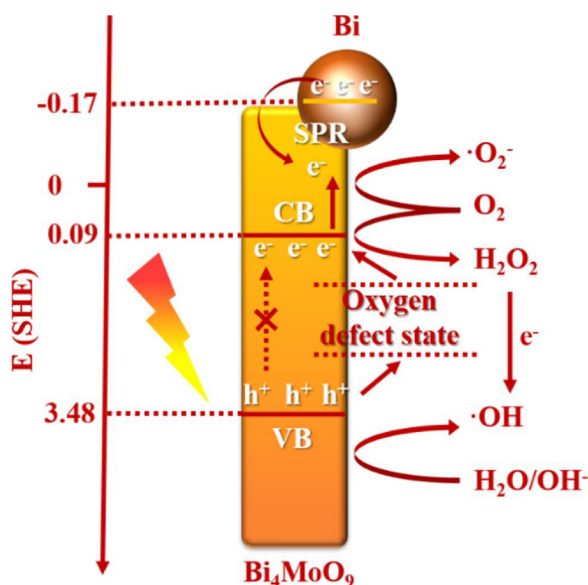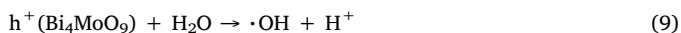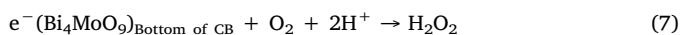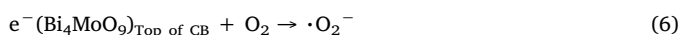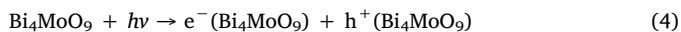Fig. 8. Photocatalysis mechanism on $Bi_4MoO_9/Bi°$ composites.

According to the above band structure analysis, the photocatalytic process over $Bi_4MoO_9/Bi°$ composites can be schematically described as Fig. 8. With the visible light illumination, the Bi_4MoO_9 core and the $Bi°$ shell will both generate pairs of active electrons and holes. Due to the more positive CB band edge of Bi_4MoO_9 than the Fermi level of $Bi°$, the electron on Bi will flow spontaneously to the CB of Bi_4MoO_9. The photoexcited electrons will react with the O_2 to generate both the $·O_2^-$ and $·OH$ radicals via different steps (See Fig. 7a), while the holes tend to react with H_2O to generate $·OH$ radicals (See Fig. 7b). Overall, $·OH$ and $·O_2^-$ radicals are the major radical species to oxidize NO into nitrates, though partial holes is proved to directly participate in NO oxidation explanted in ESR analysis.
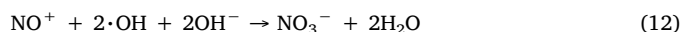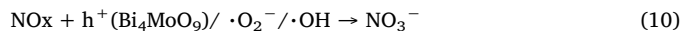
$$Bi_4MoO_9 + h\nu \rightarrow e^-(Bi_4MoO_9) + h^+(Bi_4MoO_9) \quad (4)$$

$$e^-(Bi°) \rightarrow e^-(Bi_4MoO_9) \quad (5)$$

$$e^-(Bi_4MoO_9)_{Top\ of\ CB} + O_2 \rightarrow ·O_2^- \quad (6)$$

$$e^-(Bi_4MoO_9)_{Bottom\ of\ CB} + O_2 + 2H^+ \rightarrow H_2O_2 \quad (7)$$

$$H_2O_2 \rightarrow ·OH + OH^- \quad (8)$$

$$h^+(Bi_4MoO_9) + H_2O \rightarrow ·OH + H^+ \quad (9)$$

On basis of the above mechanism and the experimental results, the enhanced photocatalytic performance of $Bi_4MoO_9/Bi°$ composites can be ascribed to the synergic effect of $Bi°$ and the oxygen vacancy. Besides the contribution to providing additional hot electrons, Bi NPs can also promote the electron/hole separation and electron lifetime in Bi_4MoO_9, by its unique SPR effect, which could trigger the formation of electromagnetic field that could affect the directional movement of hot carriers, making them not so easy to recombine. The oxygen vacancy in the core/shell structure will lead to the generation of defect states in the band gap, which enables the electrons transfer from the VB to CB by utilizing defect state as the courier station [40].

3.5. In situ DRIFT investigation on the process of photocatalytic NO oxidation

In situ DRIFTS studies were performed to understand the reaction pathway of the photocatalytic NO oxidation over the $Bi_4MoO_9/Bi°$. Fig. 9a (enlarged version in Fig. S8) shows the reaction time-dependent Infrared characteristic peak evolution under visible light irradiation. The reaction is run under a steady condition where the concentration of

NO is 50 ppm and the gas flow rate is 25 mL/min. The dark line represents the equilibrium state in Helium atmosphere was used as a reference, so that the transformation of intermediate products in photocatalytic processes can be clearly observed. After injecting the NO, a broad peak at 3453 cm^{-1} could be detected as H_2O. This peak will disappear with the light on, but immediately recover once the light is off (See Fig. 9c). It is demonstrated that the H_2O in gas component turn into $·OH$ on the surface of catalyst. And several weak absorption peaks appeared at 1347 cm^{-1}, 1507 cm^{-1} and 1612 cm^{-1} can be assigned to the adsorption of NO. When injecting pure O_2 these NO peaks turn into weak gradually as the reason of partial NO oxidation. With the irradiation of visible light, the generated band at 1178 cm^{-1} caused by vibration and rotation of bridging nitrates can be observed clearly and the intensity increased gradually over time as shown in Fig. 9e, indicating the adsorbed NO has been oxidized into NO_3^- species at the presence of $·OH$. When light on 900 s, bidentate and unidentate nitrate was observed obviously (Fig. 9a) which is a little bit unstable compared with bridging nitrates could be detected at 1017 cm^{-1} (Fig. 9d) and 1274 cm^{-1} (Fig. 9f), respectively. This result can help to understand why the activity turns down after constant irradiation a long time. At the same time, the peak at 2149 cm^{-1} was indexed as NO^+ species and achieved the highest intensity when light on (Fig. 9b). This observation means that the irradiation increased the generate rate of NO^+ species. This kind of intermediate species is produced by donating the electrons of NO to oxygen vacancy. These species are more likely to be oxidized, which enables the NO being rapidly mineralized.

In summary, the main observed IR bands of the adsorbed species and their chemical assignments are listed in supporting information (Table 2). So that the transformation of reaction product demonstrated the photocatalytic oxidation processes for NO removal directly and also further explain the effective photocatalytic activity of the Bi-loaded Bi_4MoO_9.

$$NOx + h^+(Bi_4MoO_9)/ ·O_2^-/·OH \rightarrow NO_3^- \quad (10)$$

$$NO + ·OH \rightarrow OH^- + NO^+ \quad (11)$$

$$NO^+ + 2·OH + 2OH^- \rightarrow NO_3^- + 2H_2O \quad (12)$$

4. Conclusion

In summary, this work developed one unique core/shell Bi_4MoO_9/Bi heterostructured photocatalyst with considerable number of oxygen vacancies. Compared with pure Bi_4MoO_9, the $Bi_4MoO_9/Bi°$ photocatalyst possesses better visible light absorption and lower recombination rate of the photogenerated electron/hole due to the synergistic effect of $Bi_4MoO_9/Bi°$ heterojunction, oxygen vacancy-induced defect sate and the SPR effect of Bi. Based on these merits, the $Bi_4MoO_9/Bi°$ photocatalyst exhibits highly enhanced photocatalytic activity for the NO removal under visible light irradiation in contrast to the pristine Bi_4MoO_9. The reaction pathway of the photocatalytic NO oxidation over the $Bi_4MoO_9/Bi°$ was revealed by in-situ DRFTS. The NO^+ species as a kind of new intermediate product in NO conversion is discovered and found to be critical for the conversion of NO to nitrate. Our work may shed new light on the mechanistic understanding and development of a visible-light photocatalyst for environmental applications.
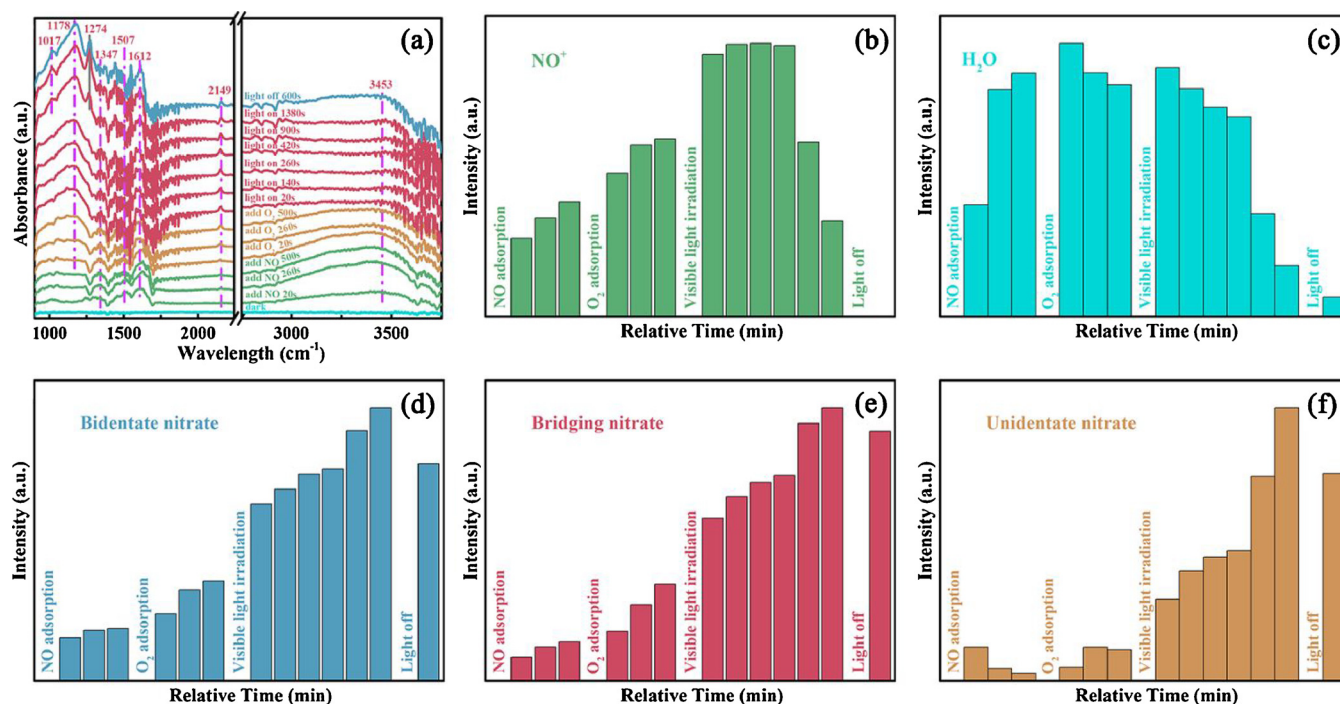
Fig. 9. In situ IR spectra of photocatalytic reaction of NO over BM-40 under visible light irradiation (a), the specific species of NO^+, H_2O, Bidentate nitrate, Bridging nitrate and Unidentate nitrate on BM-40 change over time.

Table 2

Assignments of the IR bands observed during photocatalytic NO oxidation processes over the Bi-loaded Bi_4MoO_9 under visible light irradiation.

Wavenumbers (cm^{-1})	Assignment	References
1017	Bidentate nitrate	[41]
1178	Bridging nitrate	[42]
1274	Unidentate nitrate	[43]
1347/1507/1612	NO	[44]
2149	NO^+	[42]
3453	H_2O	[44]

computational support.

Appendix A. Supplementary data

Supplementary material related to this article can be found, in the online version, at doi:https://doi.org/10.1016/j.apcatb.2018.08.064.

References

[1] M.A. Fox, M.T. Dulay, Heterogeneous photocatalysis, Chem. Rev. 93 (1993) 341–357.

[2] G. Chen, R. Gao, Y. Zhao, Z. Li, G.I. Waterhouse, R. Shi, X. Zhang, Alumina-supported CoFe alloy catalysts derived from layered-double-hydroxide nanosheets for efficient photothermal co_2 hydrogenation to hydrocarbons, Adv. Mater. 30 (2018) 1704663.

[3] G.M. Jiang, K.F. Wang, J.Y. Li, W.Y. Fu, Z.Y. Zhang, G. Johnson, X.S. Lv, Y.X. Zhang, S. Zhang, F. Dong, Electrocatalytic hydrodechlorination of 2,4-dichlorophenol over palladium nanoparticles and its pH-mediated tug-of-war with hydrogen evolution, Chem. Eng. J. 348 (2018) 26–34.

[4] G.M. Jiang, M.N. Lan, Z.Y. Zhang, X.S. Lv, Z.M. Lou, X.H. Xu, F. Dong, S. Zhang, Identification of active hydrogen species on palladium nanoparticles for an enhanced electrocatalytic hydrodechlorination of 2,4-dichlorophenol in water, Environ. Sci. Technol. 51 (2017) 7599–7605.

[5] R.Y.O.J.I. Asahi, T.A.K.E.S.H.I. Morikawa, T. Ohwaki, K. Aoki, Y. Taga, Visible-light photocatalysis in nitrogen-doped titanium oxides, Science 293 (2001) 269–271.

[6] W. Cui, J. Li, Y. Sun, H. Wang, G. Jiang, S.C. Lee, F. Dong, Enhancing ROS generation and suppressing toxic intermediate production inphotocatalytic NO oxidation on O/Ba co-functionalized amorphous carbon nitride, Appl. Catal. B-Environ. 237 (2018) 938–946.

[7] G.L. Wang, L.W. Shan, Z. Wu, L.M. Dong, Enhanced photocatalytic properties of molybdenum-doped $BiVO_4$ prepared by sol–gel method, Rare Metals 36 (2017) 129–133.

[8] Y. Zhao, B. Zhao, J. Liu, G. Chen, R. Gao, S. Yao, X. Wen, Oxide-modified nickel photocatalysts for the production of hydrocarbons in visible light, Angew. Chem. Int. Ed. 128 (2016) 4287–4291.

[9] Y. Zhao, G.I. Waterhouse, L. Zheng, X. Cao, F. Teng, T. Zhang, layered-double-hydroxide nanosheets as efficient visible-light-driven photocatalysts for dinitrogen fixation, Adv. Mater. 29 (2017) 1703828.

[10] J. Zhang, Y. Chen, X. Wang, Two-dimensional covalent carbon nitride nanosheets: synthesis, functionalization, and applications, Energy Environ. Sci. 8 (2015) 3092–3108.

[11] W.J. He, Y.J. Sun, G.M. Jiang, H.W. Huang, X.M. Zhang, F. Dong, Activation of amorphous Bi_2WO_6 with synchronous Bi metal and Bi_2O_3coupling: photocatalysis mechanism and reaction pathway, Appl. Catal. B: Environ 232 (2018) 340–347.

[12] H. Li, J. Liu, W. Hou, N. Du, R. Zhang, X. Tao, Synthesis and characterization of g-C_3N_4/Bi_2MoO_6 heterojunctions with enhanced visible light photocatalytic activity, Appl. Catal. B: Environ. 160 (2014) 89–97.

[13] W.Z. Yin, W.Z. Wang, S.M. Sun, Photocatalytic degradation of phenol over cage-like Bi_2MoO_6 hollow spheres under visible light irradiation, Catal. Commun. 11 (2010) 647–650.

[14] M. Zhang, C. Shao, P. Zhang, C. Su, X. Zhang, P. Liang, Y. Liu, Bi_2MoO_6 microtubes: controlled fabrication by using electrospun polyacrylonitrile microfibers as template and their enhanced visible light photocatalytic activity, J. Hazard. Mater. 225 (2012) 155–163.

[15] H. Wang, Y. Sun, G. Jiang, Y. Zhang, H. Huang, Z. Wu, S.C. Lee, F. Dong, Unraveling the mechanisms of visible light photocatalytic NO purification on earth-abundant insulator-based core-shell heterojunctions, Environ. Sci. Technol. 52 (2018) 1479–1487.

[16] G.H. Tian, Y.J. Chen, W. Zhou, K. Pan, Y.Z. Dong, C.G. Tian, H.G. Fu, Facile solvothermal synthesis of hierarchical flowerlike bi_2moo_6 hollow spheres as high performance visible-light driven photocatalysts, J. Mater. Chem. 21 (2011) 887–892.

[17] J. Ren, W.Z. Wang, M. Shang, S.M. Sun, E. Gao, Heterostructured bismuth molybdate composite: preparation and improved photocatalytic activity under visible-light irradiation, ACS Appl. Mater. Interfaces 3 (2011) 2529–2533.

[18] Z. Dai, F. Qin, H.P. Zhao, F. Tian, Y.L. Liu, R. Chen, Time-dependent evolution of the $Bi_{3.64}Mo_{0.36}O_{6.55}$/$Bi_2MoO_6$ heterostructure for enhanced photocatalytic activity via the interfacial hole migration, Nanoscale 7 (2015) 11991–11999.

[19] D.M. Chen, Q. Hao, Z.H. Wang, H. Ding, Y.F. Zhu, Influence of phase structure and morphology on the photocatalytic activity of bismuth molybdates, CrystEngComm 18 (2016) 1976–1986.

[20] Y. Han, L. Zhang, Y. Wang, H. Zhang, S. Zhang, Photoelectrocatalytic activity of an ordered and vertically aligned TiO_2 nanorod array/BDD heterojunction electrode, Sci. Bull. 62 (2017) 619–625.

[21] P. Chen, F. Dong, M. Ran, J. Li, Synergistic photo-thermal catalytic NO purification on MnOx/g-C_3N_4: enhanced performance and reaction mechanism, Chin. J. Catal. 39 (2018) 619–629.

[22] S.S. Rayalu, D. Jose, M.V. Joshi, P.A. Mangrulkar, K. Shrestha, K. Klabunde,

Photocatalytic water splitting on Au/TiO₂ nanocomposites synthesized through various routes: enhancement in photocatalytic activity due to SPR effect, Appl. Catal. B-Environ. 142 (2013) 684–693.

[23] R. Shi, Y. Cao, Y. Bao, Y. Zhao, G.I. Waterhouse, Z. Fang, T. Zhang, Self-assembled Au/CdSe nanocrystal clusters for plasmon-mediated photocatalytic hydrogen evolution, Adv. Mater. 29 (2017) 1700803.

[24] I. Nakamura, N. Negishi, S. Kutsuna, T. Ihara, S. Sugihara, K. Takeuchi, Role of oxygen vacancy in the plasma-treated TiO₂ photocatalyst with visible light activity for NO removal, J. Mol. Catal. A-Chem. 161 (2000) 205–212.

[25] X. Pan, M.Q. Yang, X. Fu, N. Zhang, Y.J. Xu, Defective TiO₂ with oxygen vacancies: synthesis, properties and photocatalytic applications, Nanoscale 5 (2013) 3601–3614.

[26] C. Pan, J. Xu, Y. Wang, D. Li, Y. Zhu, Dramatic activity of C₃N₄/BiPO₄ photocatalyst with core/shell structure formed by self-assembly, Adv. Funct. Mater. 22 (2012) 1518–1524.

[27] X. Peng, M.C. Schlamp, A.V.K. And, A.P. Alivisatos, Epitaxial growth of highly luminescent CdSe/CdS core/shell nanocrystals with photostability and electronic accessibility, J. Am. Chem. Soc. 119 (1997) 7019–7023.

[28] D. Pan, Q. Wang, S. Jiang, X. Ji, L. An, Synthesis of extremely small CdSe and highly luminescent CdSe/CdS core–shell nanocrystals via a novel two-phase thermal approach, Adv. Mater. 17 (2005) 176–179.

[29] K.T. Kuo, D.M. Liu, S.Y. Chen, C.C. Lin, Core-shell CuInS₂/ZnS quantum dots assembled on short ZnO nanowires with enhanced photo-conversion efficiency, J. Mater. Chem. 19 (2009) 6780–6788.

[30] M.C. Schlamp, X. Peng, A.P. Alivisatos, Improved efficiencies in light emitting diodes made with CdSe(CdS) core/shell type nanocrystals and a semiconducting polymer, J. Appl. Phys. 82 (1997) 5837–5842.

[31] F. Dong, T. Xiong, Y. Sun, Z. Zhao, Y. Zhou, X. Feng, Z. Wu, A semimetal bismuth element as a direct plasmonic photocatalyst, Chem. Commun. 50 (2014) 10386–10389.

[32] Y. Yu, C.Y. Cao, H. Liu, P. Li, F.F. Wei, Y. Jiang, W.G. Song, A Bi/BiOCl heterojunction photocatalyst with enhanced electron-hole separation and excellent visible light photodegrading activity, J. Mater. Chem. A. 2 (2014) 1677–1681.

[33] F. Dong, Q.Y. Li, Y.J. Sun, W.K. Ho, Noble metal-like behavior of plasmonic Bi particles as a cocatalyst deposited on (BiO)₂CO₃ microspheres for efficient visible

light photocatalysis, ACS Catal. 4 (2014) 4341–4350.

[34] G.M. Jiang, X.W. Li, M.N. Lan, T. Shen, X.S. Lv, F. Dong, S. Zhang, Monodisperse bismuth nanoparticles decorated graphitic carbon nitride: enhanced visible-light-response photocatalytic NO removal and reaction pathway, Appl. Catal. B-Environ. 205 (2017) 532–540.

[35] J. Shi, H.N. Cui, Z. Liang, X. Lu, Y. Tong, C. Su, H. Liu, The roles of defect states in photoelectric and photocatalytic processes for ZnₓCd₁₋ₓS, Energy Environ. Sci. 4 (2011) 466–470.

[36] F. Dong, T. Xiong, Y. Sun, L. Lu, Y. Zhang, H. Zhang, H. Huang, Y. Zhou, Z. Wu, Exploring the photocatalysis mechanism on insulators, Appl. Catal. B-Environ. 219 (2017) 450–458.

[37] M.A. Butler, D.S. Ginley, Prediction of flatband potentials at semiconductor-electrolyte interfaces from atomic electronegativities, J. Electrochem. Soc. 2 (1978) 228–232.

[38] A.H. Nethercot, Prediction of Fermi energies and photoelectric thresholds based on electronegativity concepts, Phys. Rev. Lett. 18 (1974) 1088–1091.

[39] X. Zhang, L.Z. Zhang, T.F. Xie, D.J. Wang, Low-temperature synthesis and high visible-light-induced photocatalytic activity of BiOI/TiO₂ heterostructures, J. Phys. Chem. C 17 (2009) 7371–7378.

[40] H. Li, F. Qin, Z. Yang, X. Cui, J. Wang, L. Zhang, New reaction pathway induced by plasmon for selective benzyl alcohol oxidation on BiOCl possessing oxygen vacancies, J. Am. Chem. Soc. 139 (2017) 3513–3521.

[41] D. Pozdnyakov, V. Filimonov, K. Katal, Infrared spectroscopic study of the chemisorption of nitric oxide and nitrogen dioxide on metal oxides, Kinet Katal. 14 (1973) 760.

[42] M. Iwamoto, H. Yahiro, N. Mizuno, W.X. Zhang, Y. Mine, H. Furukawa, S. Kagawa, Removal of nitrogen monoxide through a novel catalytic process. 2. Infrared study on surface reaction of nitrogen monoxide adsorbed on copper ion-exchanged ZSM-5 zeolites, J. Phys. Chem. 96 (1992) 9360–9366.

[43] K.I. Hadjiivanov, Identification of neutral and charged NxOy surface species by IR spectroscopy, Catal. Rev. 42 (2000) 71–144.

[44] K. Hadjiivanov, H. Knözinger, Species formed after NO adsorption and NO + O₂ co-adsorption on TiO₂: an FTIR spectroscopic study, Phys. Chem. Chem. Phys. 2 (2000) 2803–2806.